Influence of pre-existing configurations of dislocations on the initial pop-in load during nanoindentation in a CrCoNi medium-entropy alloy

Frederic Habiyaremye, Antoine Guitton, Xiaolei Chen, Thiebaud Richeton, Stéphane Berbenni, Florian Schäfer, Guillaume Laplanche, Nabila Maloufi

▶ **To cite this version:**

Frederic Habiyaremye, Antoine Guitton, Xiaolei Chen, Thiebaud Richeton, Stéphane Berbenni, et al.. Influence of pre-existing configurations of dislocations on the initial pop-in load during nanoindentation in a CrCoNi medium-entropy alloy. Philosophical Magazine, 2023, 104 (3), pp.137-160. 10.1080/14786435.2023.2290541 . hal-04346310

HAL Id: hal-04346310
https://hal.univ-lorraine.fr/hal-04346310v1

Submitted on 11 Oct 2024

HAL is a multi-disciplinary open access archive for the deposit and dissemination of scientific research documents, whether they are published or not. The documents may come from teaching and research institutions in France or abroad, or from public or private research centers.

L'archive ouverte pluridisciplinaire **HAL**, est destinée au dépôt et à la diffusion de documents scientifiques de niveau recherche, publiés ou non, émanant des établissements d'enseignement et de recherche français ou étrangers, des laboratoires publics ou privés.

Influence of pre-existing configurations of dislocations on the initial pop-in load during nanoindentation in a CrCoNi medium-entropy alloy

Frederic Habiyaremye[a], Antoine Guitton[a,b*], Xiaolei Chen[a,b], Thiebaud Richeton[a,b], Stéphane Berbenni[a,b], Florian Schäfer[c], Guillaume Laplanche[d], Nabila Maloufi[a,b**]

[a]Université de Lorraine–CNRS–Arts et Métiers–LEM3, 57070 Metz, France

[b]LabEx Damas–Université de Lorraine, 57073 Metz, France.

[c]Department Materials Science and Engineering, Saarland University, 66123 Saarbruecken, Germany

[d]Institut für Werkstoffe, Ruhr-Universität Bochum, Universitätsstr. 150, 44801 Bochum, Germany

*corresponding authors: * antoine.guitton@univ-lorraine.fr

**nabila.maloufi@univ-lorraine.fr

Abstract

The origin and mechanisms responsible for incipient plasticity in metals are still poorly understood. Moreover, the reasons for the recently reported large scattering of the initial pop-in load remain unclear. Hence, this study addresses these issues through a combination of nanoindentation tests and electron channeling contrast imaging characterisation considering a CrCoNi medium-entropy alloy. Experimental findings were also supported by elastic calculations that consider both the indentation and dislocation stress fields. A wide scatter in the maximum shear stress underneath the indenter, as expected, was observed for the analysis based on dislocation density. As a consequence, the spatial arrangement of dislocations within the indented region or local dislocation configuration is introduced as a new parameter to overcome overly simple analysis based on the dislocation density. The maximum shear stress underneath the indenter increased from 6 GPa for dislocation closer to the indentation axis to 11 GPa at 600 nm for dislocation far away from it. Additionally, elastic calculations revealed that the response to the incoming nanoindenter was different for dislocations with different configurations. Thus, the complex interactions of stress fields due to configurations of dislocations and indentation account for the large scatter of the maximum shear stress beneath the indenter.

Keywords

High entropy alloy, nanoindentation, electron channeling contrast imaging, plasticity, density of dislocations.

List of abbreviations

CrCoNi alloy	Chromium-Cobalt-Nickel alloy
HEA	High entropy alloy
MEA	Medium entropy alloy
ECCI	Electron channeling contrast imaging
SFE	Stacking fault energy
$\boldsymbol{g}$	Diffraction vector
P-h curve	Load-displacement curve
R	Nanoindenter tip radius
h	Displacement depth during nanoindentation
P	Applied load during nanoindentation
τ_{max}	Maximum shear stress underneath the indenter
P_p	Pop in load
G	Shear modulus
τ_{th}	Theoretical shear stress
HomND	Homogeneous nucleation of dislocation
HetND	Heterogeneous nucleation of dislocation
ρ	Global dislocation density
ρ_{loc}	Local dislocation density
PED	Pre-existing dislocation

D_{nd}	Distance between the nanoindentation axis and the nearest dislocations
a_{c}	Contact radius
RSS	Resolved shear stress
MRSS	Maximum resolved shear stress
$\bar{L}$	Mean distance between dislocations
n	Number of dislocations
A	Area of interest in the micrograph
τ_{c}	Applied resolved shear stress necessary to nucleate a dislocation loop on the active slip plane
b	Burgers vector
r_{c}	Critical loop radius
r_{o}	Dislocation core radius
p_{o}	Maximum pressure
E_r	Reduced modulus
E_s	Young's modulus of the sample
E_i	Young's modulus of the diamond nanoindenter
ν_i	Poisson's ratio of the diamond nanoindenter
ν_s	Poisson's ratio of the sample
Δh_p	Pop-in width
h_p	Pop-in depth
Δh_{hkl}	Projection of Δh_{p} along the slip direction
N_{hkl}	Number of induced dislocations emitted below an indenter

T	Temperature
e	Euler number
$\tilde{\sigma}_{ij}$	stress components of a point load applied on an elastic half-space
$\tilde{p}(x',y')$	Surface pressure distribution
FCC	Face centered cubic

1. Introduction

Contrary to conventional alloys with a single principal element and minor alloying elements, high and medium entropy alloys (HEAs and MEAs) have multiple principal elements with equal or nearly equal concentrations [1-2]. HEAs and MEAs have exceptional mechanical properties, superior to those of conventional alloys [2-5] (*e.g.*, CrCoNi MEA subjected to annealing after high-pressure torsion with an average grain size of 600 nm exhibited an ultimate tensile strength as high as 2 GPa [3]). One of the reasons behind the exceptional mechanical properties of the CrCoNi alloy has been associated with its low stacking fault energy (SFE) (22 ± 4 mJ·m^{-2}) [4]. The latter induces deformation mechanisms that improve the alloy's strength without affecting its ductility [4]. The wide separation between Shockley partials (*e.g.*, ~11 nm near edge type) initially encourages planar glide and prevents cross-slip [4]. Mechanical twinning over an extended strain range, activation of multiple slip systems, complex interactions between dislocations, dislocations and stacking faults as well as dislocations and grain (or twin) boundaries increase the degree of the work hardening rate, which simultaneously raise the strength and ductility [2-4]. Various parameters affecting the strength of CrCoNi alloy (e.g., short-range order [5], grain boundary [6]) have been investigated. For example, atomistic simulations have shown that an increase in the local chemical short-range order increases SFE and thereby raises the activation barrier governing dislocation activities [5]. While it has been proposed in several studies that initial dislocations also affect strength by controlling local plasticity [5-6], to our knowledge, the extent to which the density and configuration of the initial dislocations affect local plasticity in CrCoNi alloy has not been explored yet.

Besides measuring mechanical properties such as hardness and elastic modulus [7-8], instrumented nanoindentation is also used to probe localised deformation responses at precise locations in

materials from micro-to-nanometer length scales [9-10]. In load-controlled nanoindentation tests, one of these deformation responses is a pop-in that appears as a displacement jump on a load-displacement (*P*-*h*) curve [11]. Some crystalline materials exhibit a single pop-in, whereas others exhibit successive and multiple pop-ins [12-16]. In either case, the occurrence of the initial pop-in is linked to various mechanisms such as phase transformation [17-18], fracture with crack initiation and propagation [19], oxide film fracture [20], and dislocation-based mechanisms [21-25] among others. In metals and alloys, dislocation-based mechanisms are widely used to explain the origin of pop-ins. Accordingly, it is suggested that the pop-in marks the elastic-to-plastic transition because values of the maximum shear stress underneath the indenter at the first pop-in (τ_{max} derived from the pop-in load, P_p, see further Eq. 4 in section 2) is often in the range of the theoretical shear stress (τ_{th}), *i.e.*, between $G/25$ and $G/5$ where G is the shear modulus [22-23, 26-28]. From the values of τ_{max}, it was initially proposed that homogeneous nucleation of dislocations (HomND) is responsible for the initial pop-in [28].

The values of τ_{max} are found to significantly vary for nanoindentation tests performed in materials with different processing methods [21, 26], or deformation histories [15]. The variation of the values of τ_{max} was initially linked to the global dislocation density (ρ). Shim *et al.* [26] carried out nanoindentation in annealed, 20%, and 30% pre-strained Ni single crystals (*i.e.*, with different ρ-values). Figure 3a in [26] revealed that the annealed sample had the highest τ_{max} while the 30% pre-strained sample had the lowest τ_{max} for the same indenter radius. Furthermore, Zbib and Bahr [15] placed nanoindents along dislocation pile-ups of a large micro-indent in a W single crystal. They found that the values of τ_{max} increased from ~13 GPa near the center of the micro-indent (for nanoindents at ~5 μm with a localised $\rho = 1.8\times10^{12}$ m^{-2}) to ~21 GPa far away from the micro-indenter (for nanoindents at ~100 μm with localised $\rho = 3.5\times10^{9}$ m^{-2}). Thus, it was proposed that,

in addition to HomND, the initial pop-in can also be caused by heterogeneous nucleation of dislocations (HetND), *i.e.,* nucleation assisted by pre-existing dislocations (PEDs) or activation of pinned PEDs.

The change of τ_{max} as a function of ρ seems to be relevant for the above cases. However, it fails to explain the origin of the wide scatter of τ_{max} observed when nanoindents are performed in the same material with the same global ρ. For example, τ_{max} ranges from 14 GPa to 21 GPa for $\rho = 3.5 \times 10^9$ m^{-2} in [001]-oriented W single crystals [15], while the values of τ_{max} vary between 4 and 10 GPa in the annealed FeCoCrMnNi alloy [21]. These results demonstrate that other parameters are required, beyond the global ρ, not only to explain the origins of the wide scatter in τ_{max} but also the mechanisms responsible for the initial pop-in. Such parameters include testing temperature, crystal orientation, and local chemistry. Mridha *et al.* [22] performed nanoindentation tests at 298 K, 373 K, and 473 K in CoCrNi, CoCrFeMnNi, and $Al_{0.1}$CoCrFeNi alloys. They found that the pop-in load decreased with increasing temperature, which demonstrates a thermally activated process, where the low energy barrier for nucleation of dislocation is due to the weakening of atomic bonds promoted by thermal expansion. Seo *et al.* [30] found τ_{max} of 8.0 GPa and 10.1 GPa in the low SFE Mn austenitic steels for indentation in grains with [001] and [111] orientations, respectively. The effect of local chemistry on incipient plasticity was studied by Hua *et al.* [31] using atomistic simulations at 300 K. These authors found that dislocations are nucleated from Cr-rich nano-clusters in a CrCoNi MEA.

The above parameters should be linked to the local configuration of defects near an indent. However, it is tedious to determine the local dislocation microstructure near and below the visibility domain of the indented regions. Theoretical models [23] and numerical simulations [32-33] were used to tackle the above challenges. They suggested that the large scatter in τ_{max} depends on the

probability of finding PEDs in the sampling volume. This probability is quantified using the mean distance ($\bar{L}$) between dislocations that is determined with $\bar{L} = 1/\sqrt{\rho}$. Using the results reported for a coarse-grained CrCoNi alloy [23], with $\rho = 2.63 \times 10^{13}$ m^{-2} determined by the modified Williamson-Hall method, gives $\bar{L}$ ~195 nm. This $\bar{L}$ value is much larger than the tip contact radius (a_c, see further Eq. 6 in section 2), which is of ~52 nm. Consequently, there is a small probability of finding PEDs in the indented regions, *i.e.*, the initial pop-in is more likely to result from HomND. Furthermore, $\bar{L}$ was also used to explain why the large indenter tip had lower τ_{max}-values than the small indenter tip. The nanoindentation tests carried out with a large tip radius have a large sampling volume, which is more likely to contain PEDs, whereas the sampling volume is small and may not contain any PEDs with a small tip radius [26]. In agreement with $\bar{L}$, Morris *et al*. [32] used a statistical model assuming that an ideal τ_{max} (denoted $\tau_{max,\,I}$) is required to initiate the pop-in. If there is no defect in the sampling volume, then $\tau_{max} = \tau_{max,\,I}$ (the initial pop-in occurs by HomND), and, if there is a defect, then $\tau_{max} < \tau_{max,\,I}$ (the initial pop-in occurs by HetND). Similarly, Engels *et al*. [33] developed a lower-order non-local crystal plasticity model, based on geometrically necessary dislocations, to show that the presence of PEDs at some distance from the indenter reduces τ_{max}. The limitations of both ρ and $\bar{L}$ in explaining the pop-in lies in the fact that they are based on theoretical/numerical predictions rather than actual experimental observations. While the predictions can be relevant for simple configurations such as a homogenous distribution of defects, it fails to explain the pop-in in cases of complex configurations of defects such as a pair of dislocations, a dislocation dipole, or a wall of dislocations. These configurations are frequently observed in plastically deformed alloys.

This is the background of the current study, where the results from the experiments (nanoindentation tests and electron channelling contrast imaging (ECCI)) and elastic calculations

are reported. The experimental part has three objectives: (1) to investigate the influence of the localised ρ on the scatter of the values of τ_{max}, (2) to study the influence of the local dislocation configurations on the scatter of the values of τ_{max}, and (3) to propose possible mechanisms of incipient plasticity in CrCoNi medium entropy alloy. The elastic calculations are based on the superposition principle in linear elasticity to compute the stress fields due to the indenter and dislocations. They have two objectives. First, they are used to qualitatively explain and support the analysis and interpretation of the experimental results. Second, they are used to assess the influence of various configurations of dislocations such as a pair of dislocations or a dislocation dipole that are not distinguishable in our experiments from ECC micrographs.

2. Material and methods

The material used in this study is the single crystalline CrCoNi MEA processed by the Bridgman method as described in [34-36]. The cylindrical sample with a base diameter of 12 mm and a height of 8 mm was initially cut at 90° from the growth axis. It was then subjected to mechanical polishing down to 1 µm using diamond suspension. It was finally chemo-mechanically polished with an aqueous mixture of hydrogen peroxide and oxide suspension. Microstructures before and after nanoindentation were acquired with the ECCI inside a Zeiss Auriga FIB-FEGSEM (Oberkochen, Germany), with a working distance of 6.2 mm and voltage of 20 kV. ECCI is a powerful technique that provides access to dislocation scale micrographs and allows the characterisation of crystalline defects such as dislocations, stacking faults, and grain boundaries at a depth of ~100 nm below a bulk sample surface [37-38]. Further details about ECCI allowing a fine characterisation of defects are given in [39-43].

Instrumented nanoindentation was conducted using a sharp Berkovich indenter tip (Synton-MDP AG, Switzerland) inside the Hysitron TI-900 nanoindentation machine (Bruker, USA). The load-

controlled tests were carried out up to a maximum load of 500 µN and 1000 µN for 54 and 36 indents, respectively. Maximum loads of 500 µN and 1000 µN were utilized to determine if the value of the maximum load had an effect on the initial pop-in load. According to the findings, the maximum load did not affect the initial pop-in load. The indentation spacings of 3 µm and 5 µm for indents at 500 µN and 1000 µN were three times the lateral size of the residual imprints of 1 µm and 1.5 µm, respectively, to avoid the influence of one indent on the other [44]. A number of 30 indents were selected from the two arrays based on their locations inside the subgrains to ensure that low-angle grain boundaries do not influence the nanoindentation test [45].

3. Results

3.1. Experiment

Figure 1a depicts a representative *P-h* curve for an indent in the single crystal. It shows that the first part is purely elastic as it matches the Hertz elastic theory of a sphere in contact with a semi-infinite space (see the red dashed curve in Fig. 1a). Indeed, in this theory, the applied load (P) is governed by:

$$P = \frac{4}{3} E_r \sqrt{R h^3} \tag{1}$$

where h is the displacement of the nanoindenter, R is the nanoindenter tip radius, and E_r is the reduced elastic modulus. Assuming isotropic elasticity, E_r is obtained from:

$$\frac{1}{E_r} = \frac{1-\nu_i^2}{E_i} + \frac{1-\nu_s^2}{E_s} \tag{2}$$

where E_i (= 1141 GPa) and ν_i (= 0.07), E_s (= 235 GPa) and ν_s (= 0.31) are Young's moduli and Poisson's ratios of the diamond nanoindenter and the CrCoNi MEA sample, respectively [46]. Therefore, E_r~212 GPa from equation (2). Then, the average value of R obtained from equation (1)

is ~220 nm. On the *P-h* curve in Fig. 1a, the end of the elastic portion is characterised by an initial pop-in that occurs at a load (P_p) of 203.4 µN and a depth (h_p) of 13.45 nm. The difference between the beginning and the end of the pop-in is 6.91 nm and is referred to as the pop-in width (Δh_p). Both h_p and Δh_p increase with the pop-in load as shown in Fig. 1b. This plot is consistent with the ones reported by Schuh and Lund [47] in 4H SiC, Pöhl [20] in polycrystalline pure iron and Sekido *et al.* [24] in steels. The values of h_p are linked to mechanisms responsible for the initial pop-ins, while the values of Δh_p are related to the number N_{hkl} of induced dislocations emitted below the indenter in a subgrain with a given *hkl* orientation [48-49]:

$$N_{hkl} = \frac{\Delta h_{hkl}}{|\mathbf{b}|} \tag{3}$$

where Δh_{hkl} is the projection of Δh_p along the slip direction and **b** is the Burgers vector.

The microstructures of the single crystals processed Brigdman method were reported in [45, 50-51]. Figures 2 display ECC micrographs before and after nanoindentation, along with a plot of load-indentation depth. A majority of the dislocations are threading dislocations that appear as spots with dark and bright contrast as shown in Figs. 2a-b, *i.e.*, dislocations nearly perpendicular to the observation surface [45, 52]. Threading dislocations do not go out of contrast under different diffraction vectors, ***g*** unlike inclined dislocation [45]. In addition, the resolved shear stress on threading dislocations due to the nanoindenter is very small, and thus threading dislocations are unlikely to be pushed by the stress field of the nanoindenter. There are also a few slightly inclined dislocations with contrast that starts with a bright spot at their intersections with the surface which is followed by a line that progressively fades with the depth in a crystal (see red rectangle in Fig. 2a) [37,43, 53]. Moreover, thick bright lines (as shown by red arrows in Figs. 2a-b) correspond to stacking faults. Stacking faults' contrast using ECCI has been modelled in [40,55] and observed in [45,54]. Initially appearing as a bright and intense line at the intersection with the sample surface,

it rapidly dissipates and demonstrates weak, yet distinctive oscillations that result from the profiles of backscattering electron intensity across the faults. The amplitude of oscillations decreases as the distance from the stacking fault and surface intersection increases. This phenomenon is attributed to Bloch wave absorption [40, 55].

The local pre-existing dislocation density (ρ_{loc}) can be estimated using Figs. 2a-b. Generally, it is calculated as a ratio of the number of dislocations (n) intersecting the surface over an area (A) [56]. Since there are mainly threading dislocations, $\rho_{loc} = n/A$. Using dislocations enclosed by red circles as references, the ρ_{loc} value is estimated by superimposing the microstructure before and after nanoindentation and drawing a circle around the plastically deformed zone after nanoindentation (a region bounded by a bright region on an ECC micrograph), and then counting n in that zone before nanoindentation (see white circles in Figs. 2a-b).

Since the distribution of preexisting dislocations is known before nanoindentation, the distance between the indentation axis and the nearest dislocation (D_{nd}) is introduced as a new spatial parameter beyond ρ_{loc}. It was measured using two steps. Initially, the two micrographs before and after nanoindentation from the same location are superimposed to locate the center of the residual nanoindent on the micrograph before nanoindentation (Fig. 3). Then, D_{nd} is measured by considering the closest visible dislocation to the center of the residual imprint (Figs. 3a and c). Given that the threading dislocations are nearly parallel to the indentation axis and that the pop-in depth h_p is lower than 17 nm in our experiments, whereas the defect observation depth of ECCI is ~100 nm [57], it is reasonable to assume that the observed dislocations at the surface from ECC micrographs are those that may affect the indentation response.

The values of P_p decrease with increasing values of ρ_{loc} as depicted by the curve in Fig. 4a. This trend is consistent with a power-law relationship of the form, $P_p \sim 3.1 \times 10^5 \times \rho_{loc}^{-0.27}$. The reason for the general decrease of the initial pop-in load with the localised dislocation density has been explained theoretically from the increase in the probability to find PEDs in the indented volume (see the introduction). PEDs have their own stress fields that contribute to the stress fields coming from the nanoindenter. For instance, the high ρ_{loc} lead to lower P_p due to the interaction between stress fields from the incoming indent and stress fields from one or more PEDs in the indented regions. Nucleation of dislocations occurs heterogenous by multiplication and motion of PEDs. On the other hand, P_p increased when ρ_{loc} decreased because there were no PEDs present in the indented regions or they were too far from the indented regions to have a substantial impact. Thus, nucleation of dislocations occurs homogeneously at high P_p . A detailed figure that corresponds to Fig. 4a has been added in supplementary data as Fig. S1.

Slightly different power-law relationships of the form, $P_p = \rho^{-0.5}$ (ρ being determined as the density of etch pits) and $P_p = s \times \rho^{-0.5} + t$ (where s and t are constants, ρ being the density of Frank-Read sources that are randomly distributed throughout the simulation box) were previously reported in [15,49]. The dislocation activation model used in [15] was limited by two fitted experimental data points and a range of ρ from 1×10^{12} m^{-2} to 2×10^{12} m^{-2}. Employing a three-dimensional dislocation dynamics-finite element method simulator, Crone *et al*. [49] improved the number of data points to four and a range of ρ from 1.25×10^{12} m^{-2} to 8×10^{13} m^{-2}. However, the number of data points was still too low to define a reliable power law for the relationship between ρ and P_p. Although one can argue that ρ and P_p are linked by a power-law based on experimental and numerical results in the literature, these results are limited in terms of ρ range to produce an acceptable and reliable fitting model. Our results clearly show a very strong trend

between the measured P_p values and ρ even if further experiments with access to a wide range of ρ, for example 10^7- 10^{14} m^{-2} , are needed to capture the scatter.

Given P_p, the maximum principal shear stress τ_{max} beneath the surface can be estimated using a standard Hertz normal contact theory assuming isotropic linear elasticity [58]. From the expression of the maximum pressure p_0 (see [58], Chapter 4, p. 93), τ_{max} is given by:

$$\tau_{max} = 0.31\, p_0 \text{ with } p_0 = \left(\frac{6E_r^2 P_p}{\pi^3 R^2}\right)^{\frac{1}{3}} \quad (4)$$

Replacing P_p values, the resulting values of τ_{max} are between 6 and 11 GPa which are within τ_{th} range, *i.e.*, $G/25$ = 3.6 GPa and $G/5$ = 18 GPa (G = 90 GPa for CrCoNi [46]). These values are comparable to τ_{max} between 5.2 GPa and 9 GPa obtained in the coarse-grained CrCoNi alloy [22]. These values suggest that the incipient plasticity may be related to the nucleation of dislocations [21-25]. To assess the HomND, a model developed by Hirth and Lothe [59], expanded by Michalske and Houston [60], and Chiu and Ngan [61] was used. In the latter, the applied resolved shear stress on the active slip plane (τ_C) required to nucleate an edge dislocation loop of critical radius, r_c, and where **b** is perpendicular to the loop plane at 0 K was given by [62]:

$$\tau_C = \frac{G|\mathbf{b}|}{(1-\nu)\,\pi\, e\, r_0} \quad (5)$$

where r_0 is the dislocation core radius (r_0 reasonably lies in the range |**b**| to 4|**b**| [58]), ν is the Poisson s ratio and e is the Euler number and $r_c = e r_0/2$). The derivation of equation (5) from the free energy of formation for a dislocation loop in the presence of applied shear stress has been treated in Ref. [63]. By replacing relevant values for CrCoNi MEA and assuming $r_0 = 2|\mathbf{b}|$ [58], |**b**|= 0.253 nm, τ_C is around 7.6 GPa which is equivalent to τ_{max} at 0 K. At room temperature, the thermal contribution lowers τ_{max} because nucleation of dislocation is a thermally activated event

[64-65]. To our knowledge, no studies in the literature quantified the variation of τ_{max} with temperature in CrCoNi MEA. Hence, we rely on studies on CrMnFeCoNi alloy to link τ_{max} at 0 K and room temperature because they have a slightly comparable crystal structure, chemical complexity, and mechanical properties [4]. Relying on nanoindentation tests at 295 K, 325 K, 373 K, and 423 K as well as extrapolation, Zhu *et al.* [29] came up with a rough relationship $\tau_{max} = -0.00728T + 8.01$ where T is the temperature in K. Using the relation, τ_{max} at 293 K is approximated to 5.5 GPa which is still within the range of τ_{th}.

Moreover, a plot of τ_{max} against ρ_{loc} (Fig. S2 in supplementary data) shows the same trend as P_p against ρ_{loc}. A close look at the plot reveals that τ_{max} can take significantly different values for the same values of ρ_{loc}, for example, τ_{max} takes the value of 7 GPa or 10 GPa for $\rho_{loc} = 1.37 \times 10^{12}$ m^{-2}. This scattering in the τ_{max} values have been also reported in [10].

A plot of τ_{max} against D_{nd} depicted in Fig. 4b shows that τ_{max} increases with D_{nd} following a power law of the form: $\tau_{max} \approx 4.8 \times D_{nd}^{0.12}$. The area beneath the indenter tip at τ_{max} is calculated from the contact radius a_c obtained from Hertz's normal contact theory [58]:

$$a_c = \left(\frac{3P_p R}{4E_r}\right)^{\frac{1}{3}} \tag{6}$$

Replacing values from the experiment, the average a_c is between 45-55 nm. Given this small a_c, HomND seems to be responsible for the initial pop-in for the nanoindent at $D_{nd} > 400$ nm and τ_{max} approaching τ_{th}. The decrease of τ_{max} when D_{nd} becomes smaller has been linked to HetND due to PEDs, stacking faults, impurities, etc. The first mechanism states that incipient plasticity occurs by the activation of PEDs, when the latter are mobile [58]. The second mechanism occurs by HomND but the pre-existing stress field reduces both maximum principal shear stress τ_{max} and h_p. Even if only one nearest dislocation is considered for micrographs in Fig. 3, the ECC micrograph in Fig.

3a shows that there are other dislocations at distances close to D_{nd} which may additionally increase the pre-existing shear stress beneath the indenter.

Figure 5a shows a detailed plot of Fig. 4b. The four square-shaped points show nanoindents that were placed where the nearest dislocation configuration (see red ellipsis in Fig. 3c) was either a pair of dislocations (two parallel dislocations with the same ***b*** (see the schematic in Fig. 5b)) or a dislocation dipole (two parallel dislocations with opposite ***b*** (see the schematic in Fig. 5c)). These nanoindents exhibited higher high P_p (Fig. 3e) and τ_{max} than their counterparts at the same D_{nd}.

3.2. Stress field calculations

Three-dimensional (3D) elastic calculations were performed using the principle of superposition in linear homogeneous isotropic elasticity. The resolved stress field at an arbitrary point (x, y, z) is assumed to be the sum of the indentation and dislocation stress fields. The stress fields generated by the axisymmetric nanoindenter under contact with the surface are obtained by employing a double integration on the spherical contact surface with the hypothesis that the real contact area between the indentation tip and the surface can be treated as circular. The integrals are derived from Johnson's contact mechanics-based equations (3.19) [58]. These equations describe the stress components ($\tilde{\sigma}_{ij}$) of a point load applied on an elastic half-space. The ratio of the stress components at some arbitrary position (x, y, z) to the maximum contact pressure p_o is thus calculated using the following integration [58,65]:

$$\frac{\tilde{\sigma}_{ij}\left(\frac{x}{a_c},\frac{y}{a_c},\frac{z}{a_c}\right)}{p_o}=\int_0^{a_c}\int_0^{2\pi}\tilde{p}(x',y')\tilde{\sigma}_{ij}\left(\frac{x}{a_c}-x',\frac{y}{a_c}-y',\frac{z}{a_c}\right)rd\theta dr \quad (7)$$

where $x' = r\cos\theta$, $y' = r\sin\theta$, the components of $\tilde{\sigma}_{ij}$ are reported in the Appendix and the maximum contact pressure p_o for a circular contact of radius a_c was reported in equation (4). It

describes the elastic regime until the incipient plasticity occurs during loading. The surface pressure distribution, $\tilde{p}(x',y')$, is computed from the following relation:

$$\tilde{p}(x',y') = \sqrt{1 - \frac{x'^2 + y'^2}{a_c^2}} \tag{8}$$

The stress fields due to an infinite straight-edge dislocation in a homogeneous infinite medium are well-known in isotropic elasticity, see, e.g., the expressions in [58]. The dislocation self-stress field is considered to be zero at the dislocation position. The dislocation core radius is assumed to be $|3\boldsymbol{b}|$ [56]. Moreover, the dislocation is regarded as an infinite straight line parallel to z where x and y are the contact surface in an orthonormal cartesian frame, as shown in Fig. 6. The parameters used for the calculations are displayed in Table 1. The elastic constants of the sample and the diamond tip are given in Section 3.1.

A 3D volume was chosen for the calculations. The loading force (P_p in equation (4)) was gradually increased for either indentation alone or indentation with different dislocation configurations until the maximum resolved shear stress (MRSS) reaches a preset value of 11 GPa, which corresponds to the maximal value of τ_{max} observed experimentally (see Figs. 4b and 5). In the calculations, the value of the resolved shear stress (RSS) is assumed to be obtained using a Tresca-like criterion as half the difference between the maximal and minimal principal stresses. The incremental step of P_p is 1 μN. The P_p values that give the MRSS for different combinations of dislocations and indentation are used to calculate τ_{max} using equation (4). Of the numerous possibilities of dislocation configurations, we have limited ourselves to the cases of a single dislocation, a pair of dislocations, and a dislocation dipole. These configurations are placed at pre-defined distances from the position of the nanoindentation axis. A contour plot of the RSS field in the x-z plane due to indentation alone showed that the MRSS occurs at a depth of ~25 nm (Fig. 7a), which is

consistent with a theoretical value of ~ 0.48a_c [66]. Figure 7b depicts the distribution of the RSS at a depth of ~ 25 nm in the *x*-*y* plane for indentation stress field alone. It shows that the MRSS is located at the indentation axis and the magnitude of the resolved shear stress decreases moving away from the center.

Figures 7c-d show infinite straight-edge dislocations with **b** = ½ [10-1] and **b** = ½ [011] placed at the indentation axis. By comparing the contour plots of nanoindentation plus a dislocation with **b** = ½ [10-1] (Fig. 7c) and a dislocation with **b** = ½ [011] (Fig. 7d), it is observed that different Burgers vectors yield different distributions of RSS and position of MRSS. For the case of two dislocations, *e.g.*, a pair of dislocations or a dipole, they were placed 2 nm apart. For two dislocations at (0,0) nm and (2,0) nm with **b** = ± ½ [10-1], the contour plots showed different interactions of its constituent dislocations (Fig. 7e-f). The MRSS position was around the edge of the dislocations at (2,0) position for a pair of dislocations, whereas it was between the two dislocations for a dipole.

Fig. 8 displays τ_{max} against D_{nd} for different configurations of dislocations. It shows that with some dislocation configurations, with the increase of the distance between the dislocation and the indentation axis, τ_{max} first slightly decreases (over a small distance, except for the dislocation dipole case) and then increases when the dislocation goes far away from the indentation axis. This result is in qualitative agreement with Fig. 4b. The curve starts to level off at a distance of around 55-65 nm, beyond which only the indentation stress fields contribute to τ_{max}. The zoomed transition area (see Fig. 8) shows that the transition distance and the corresponding τ_{max} are different for different dislocation configurations, even if the differences are weak. However, it should be highlighted that the maximum value of τ_{max} is reached at much smaller D_{nd} values than in the experiment (see Figs. 4b and 5).

4. Discussions

ECCI characterization offers micrographs at the dislocation scale, both before and after deformation, facilitating an investigation into the effect of local microstructural features on the localised plastic deformation in a CrCoNi MEA. Previous studies relying on the global dislocation density showed a wide scatter of values of maximum shear stress underneath the indenter (τ_{max}) in different metallic materials [15, 21, 26]. Like previous studies based on global dislocation density, the results of our study indicate that the values of τ_{max} decrease as the local dislocation density (ρ_{loc}) increases. The potential explanation supported by our ECC micrographs in Figs. 2 and 3 is that during nanoindentation, there are more dislocations interacting with incoming indent in a region with a high ρ_{loc} when compared with a region with a low ρ_{loc}. Nevertheless, we noticed also a significant difference in the values of τ_{max} for the same values of ρ_{loc}. Upon close examination of the ECC micrographs, it was observed that there were varying spatial configurations of dislocations within the indented zone despite having the same values of ρ_{loc}. Such observation highlights the need to go beyond ρ_{loc} in order to determine the underlying causes of the wide scattering of the values τ_{max}.

The distance between the nanoindentation axis and the nearest defect ($D_{nd)}$ was determined from on the spatial configuration of dislocations observed in ECC micrographs. While the values of τ_{max} increase with $D_{nd,}$ there are still a noticeable a scatter of data. However, the scatter was not as significant as the case ρ_{loc}. While our primary focus was on measuring D_{nd} at the nearest dislocation, it is essential to recognize the influence of other dislocations closer to D_{nd} on nanoindentation tests. Furthermore, it is likely that vacancies exist within the indented regions where dislocation nucleation can occur [63]. This is because there are few sinks available for

vacancy annihilation during cooling to room temperature for single crystals [63]. Temperature was also reported to reduce the values of τ_{max} by lowering the activation energy barrier for dislocation nucleation [29, 64]. Therefore, it is possible that the complex and multiple interactions between incoming nanoindenter with defects such as vacancies, stacking faults, and other dislocations at varying distances from the indenter enhanced by temperature rise is responsible for the scatter of the values of τ_{max}.

It is very difficult to isolate the effect of a single microstructural feature such as a single dislocation during a nanoindentation experiment. Thus, elastic calculations were used because it allows us to solely assess the effect of dislocation at a pre-defined distance from the indentation axis (D_{nd}) without the effect of other parameters (perfect crystal). They globally showed that the apparent τ_{max} increase with D_{nd} up to a certain distance which agrees with the experiment. Moreover, they show that the values τ_{max} are affected the nature of dislocations (*e.g.*, different burgers vectors) as well as their configuration (*e.g.*, pair of dislocations or dislocation dipole) (see Fig. 8). While elastic calculations provided insights for simple configurations, it may be interesting in future studies to look at the influence of complex configuration such as arrays of dislocations (low angle grain boundaries or pile-ups), different dislocation densities with random distributions (concomitant contribution of multiple dislocations at different distances to the indentation axis), etc. Our elastic calculations revealed that beyond D_{nd}, the nature and configuration of dislocations play a role in the wide scatter of values of τ_{max}.

While experimental τ_{max} marks the elastic-to-plastic transition, it does not specify which mechanism is responsible for it. However, present elastic calculations and experimental results show that it is due to dislocation-based mechanisms as reported in the literature [23-24, 66-67]. Initial ρ-based explanations for mechanisms for the pop-in that relied on the probability of finding

PEDs below the indenter [10] failed to explain a wide distribution of τ_{max} in the regions with the same ρ. Indeed, the probability of finding PEDs increases with ρ if it is assumed that PEDs are homogeneously distributed, which is not always the case. Thus, the ρ-based explanation only partially explains the pop-in because it does not consider the case where dislocations have a particular configuration, especially their polarity or the distance between individual dislocations (a single dislocation, a dislocation dipole, or a pair of dislocations) beneath the indenter, nor the case where a dislocation or multiple dislocations are at different distances from the indenter. Our study shows that the wide statistical distribution τ_{max} and mechanisms responsible for the pop-in are mainly rooted in the nature and local configuration of dislocations or/ and other defects as well as their relative position to the nanoindentation axis. However, more than one dislocation along with other defects such as point defects affect the value of τ_{max} which makes it difficult to isolate individual cases. Based on both the experiment and elastic calculations, there are two cases. When the PED is close to the indentation axis, τ_{max} occurs at the position of dislocation, *i.e.*, incipient plasticity is due to activation of the PED. When the dislocation is far away from the indentation axis τ_{max} approaching τ_{th} occurs at the indentation axis, *i.e.*, incipient plasticity is due to homogeneous nucleation of dislocations.

5. Conclusions

Electron channeling contrast imaging (ECCI), nanoindentation test and elastic calculations were used to investigate the effect of nature and spatial configurations of dislocations on the scattering of the maximum shear stress beneath the indenter (τ_{max}) and possible mechanisms of incipient plasticity in CrCoNi medium entropy alloy. The main conclusions of this study are as follows:

- The values of τ_{max} decreases with increasing ρ_{loc} . However, a scatter was observed indent placed in the region with the same ρ_{loc} , *i.e.*, cannot explain the origins of the scatter of the values of τ_{max}.
- The reasons for the wider scatter of the values of τ_{max} are complex interactions of stress fields due to the nature and spatial configurations of dislocations and possibly other defects pre-existing in the indented zone.
- Mechanisms responsible for the initial pop-in are homogeneous and heterogeneous nucleation of dislocations, which are controlled by D_{nd} and different nature and configurations of defects near the indentation axis.

This study reveals that an initial pop-in is a complex event that is concomitantly controlled by a wide range of local microstructural features. While this study emphasizes the role of static and simple dislocation configuration, other defects such as vacancies, and crystallographic orientation may play a role in the initial pop-in load. Therefore, further experimental or elastic calculation studies incorporating all or some of these complex microstructural features are needed to understand plasticity induced by nanoindentation in metallic materials. This study has partially clarified the origin and mechanisms in the earlier stages of plasticity in MEAs and HEAs. It also provides insight into the local plastic deformation of low SFE materials such as austenitic stainless steels.

Appendix

Stress components at some arbitrary position (x, y, z) due to a concentrated normal point force p_0 acting on the surface of an elastic half-space are given by contact mechanics equations of Johnson [62] and has been reported by Caër et al. [65].

$$\tilde{\sigma}_{xx}=\frac{1}{2\pi}\left[\frac{1-2\nu}{r^2}\left\{\left(1-\frac{z}{\rho}\right)\frac{x^2-y^2}{r^2}+\frac{zy^2}{\rho^2}\right\}-\frac{3zx^3}{\rho^5}\right]$$

$$\tilde{\sigma}_{yy}=\frac{1}{2\pi}\left[\frac{1-2\nu}{r^2}\left\{\left(1-\frac{z}{\rho}\right)\frac{y^2-x^2}{r^2}+\frac{zy^2}{\rho^2}\right\}-\frac{3zy^3}{\rho^5}\right]$$

$$\tilde{\sigma}_{zz}=\frac{3}{2\pi}\frac{z^3}{\rho^5}$$

$$\tilde{\sigma}_{xy}=\frac{1}{2\pi}\left[\frac{1-2\nu}{r^2}\left\{\left(1-\frac{z}{\rho}\right)\frac{xy}{r^2}-\frac{xyz}{\rho^3}\right\}-\frac{3xyz}{\rho^5}\right]$$

$$\tilde{\sigma}_{xz}=-\frac{3}{2\pi}\frac{xz^2}{\rho^5}$$

$$\tilde{\sigma}_{yz}=-\frac{3}{2\pi}\frac{yz^2}{\rho^5}$$

Acknowledgments

G. L. acknowledges funding from the Deutsche Forschungsgemeinschaft through project B8 of the SFB/TR 103.

References

[1] C.G. Gao, J.W. Yeh, P.K. Liaw, Y. Zhang, H*igh Entropy Alloys: Fundamentals and Applications,* Springer International Publishing, Switzerland, 2016.

[2] B. Gludovatz, A. Hohenwarter, K.V. Thurston, H. Bei, Z. Wu, E.P. George, R.O. Ritchie, *Exceptional damage-tolerance of a medium-entropy alloy CrCoNi at cryogenic temperatures*, Nat. Commun. 7 (2016), pp. 1-8.

[3] P. Sathiyamoorthi, J. Moon, J. W. Bae, P. Asghari-Rad, H. S. Kim, *Superior cryogenic tensile properties of ultrafine-grained CoCrNi medium-entropy alloy produced by high-pressure torsion and annealing*, Scr. Mater. 163 (2019), pp. 152–156.

[4] G. Laplanche, A. Kostka, C. Reinhart, J. Hunfeld, G. Eggeler, E. P. George, *Reasons for the superior mechanical properties of medium-entropy CrCoNi compared to high-entropy CrMnFeCoNi*, Acta Mater. 128 (2017), pp. 292–303.

[5] X. Yang, Y. Xi, C. He, H. Chen, X. Zhang, S. Tu, *Chemical short-range order strengthening mechanism in CoCrNi medium-entropy alloy under nanoindentation*, Scr. Mater. 209 (2022), pp. 114364.

[6] D.Q. Doan, A.S. Tran, and N.C. Vu, *Grain and twin boundaries dependent mechanical behaviour of FeCoCrNiCu high-entropy alloy*, Mater. Today Commun. 34 (2023), pp. 104975.

[7] G. Oliver, W.C. Pharr, *An improved technique for determining hardness and elastic modulus using load and displacement sensing experiments*, J. Mater. Res. 7 (6) (1994), pp. 1564–1583.

[8] W. C. Oliver, G. M. *Pharr, Measurement of hardness and elastic modulus by instrumented indentation: Advances in understanding and refinements to methodology*, Mater. Res. Soc. 19 (1) (2004), pp. 3-20.

[9] D. F. Bahr, D. E. Kramer, W. W. Gerberich, *Non-linear deformation mechanisms during nanoindentation*, Acta Mater. 46 (10) (1998), pp. 3605–3617.

[10] C. Tromas, P. Villechaise, S. Dubois, *Slip line analysis around nanoindentation imprints in Ti_3SnC_2: a new insight into plasticity of MAX-phase materials*, Philos. Mag. 91 (7-9) (2011), pp. 1265-1275.

[11] D. Lorenz, A. Zeckzer, U. Hilpert, P. Grau, H. Johansen, H. S. Leipner, *Pop-in effect as homogeneous nucleation of dislocations during nanoindentation*, Phys. Rev. B 67 (17) (2003), pp. 1– 4.

[12] Y. Xia, Y. Gao, G. M. Pharr, H. Bei, *Single versus successive pop-in modes in nanoindentation tests of single crystals*, J. Mater. Res. 31 (14) (2016), pp. 2065–2075.

[13] N. Zhou, K. I. Elkhodary, X. Huang, S. Tang, Y. Li, *Dislocation structure and dynamics govern pop-in modes of nanoindentation on single-crystal metals*, Philos. Mag. 100 (12) (2020), pp. 1585–1606.

[14] H. Bei, Y. F. Gao, S. Shim, E. P. George, G. M. Pharr, *Strength differences arising from homogeneous versus heterogeneous dislocation nucleation*, Phys. Rev. B 77 (6) (2008), pp. 2–5.

[15] A. Zbib, D. F. Bahr, *Dislocation nucleation and source activation during nanoindentation yield points*, Metall. Mater. Trans. A 38 (2007), pp. 2249–2255.

[16] A. Gouldstone, H. J. Koh, K. Y. Zeng, A. E. Giannakopoulos, S. Suresh, *Discrete and continuous deformation during nanoindentation of thin films*, Acta Mater. 48 (9) (2000), pp. 2277–2295.

[17] D. Chrobak, K. Nordlund, R. Nowak, *Nondislocation origin of GaAs nanoindentation pop-in event*, Phys. Rev. Lett. 98 (2007) pp. 1-4**.** h

[18] G. Laplanche, J. Pfetzing-Micklich, G. Eggeler, S*udden stress-induced transformation events during nanoindentation of NiTi shape memory alloys*, Acta Mater. 78 (2014), pp. 144–160.

[19] B. Bor, D. Giuntini, B. Domènech, M. V. Swain, G. A. Schneider, *Nanoindentation-based study of the mechanical behavior of bulk supercrystalline ceramic-organic nanocomposites*, J. Eur. Ceram. Soc. 39 (10) (2019), pp. 3247–3256.

[20] D. Rodriguez-Marek, M. Pang, D. F. Bahr, *Mechanical measurements of passive film fracture on an austenitic stainless steel*, Metall. Mater. Trans. A 34 (2003), pp. 1291–1296.

[21] D. Wu, J.S.C. Jang, T.G. Nieh, *Elastic and plastic deformations in a high entropy alloy investigated using a nanoindentation method*, Intermetallics, 68 (2016), pp. 118-127.

[22] S. Mridha, M. Sadeghilaridjani, S. Mukherjee, *Activation volume and energy for dislocation nucleation in multi-principal element alloys*, Metals, 9 (2) (2019), pp. 263.

[23] S. Sun, Y. Yang, C. Han, G. Sun, Y. Chen, H. Zong, J. Hu, S. Han, X. Liao, X. Ding, J. Lian, *Unveiling the grain boundary-related effects on the incipient plasticity and dislocation behavior in nanocrystalline CrCoNi medium-entropy alloy*, J. Mater. Sci. Technol. 127 (2022), pp. 98-107.

[24] K. Sekido, T. Ohmura, L. Zhang, T. Hara, K. Tsuzaki, *The effect of interstitial carbon on the initiation of plastic deformation of steels*, Mater. Sci. Eng. A 530 (1) (2011), pp. 396–401.

[25] F. Pöhl, *Pop-in behavior and elastic-to-plastic transition of polycrystalline pure iron during sharp nanoindentation,* Sci. Rep. 9 (2019) pp. 1-12.

[26] S. Shim, H. Bei, E. P. George, G. M. Pharr, *A different type of indentation size effect*, Scr. Mater. 59 (2008) pp. 1095–1098.

[27] K. Gan, D. Yan, S. Zhu, Z. Li, 2021, *Interstitial effects on the incipient plasticity and dislocation behavior of a metastable high-entropy alloy: Nanoindentation experiments and statistical modeling*, Acta Mater. 206 (2021) pp. 116633.

[28] R.D.K. Misra, Z. Zhang, Z. Jia, M.C. Somani, L.P. Karjalainen, *Probing deformation processes in near-defect free volume in high strength–high ductility nanograined/ultrafine-grained (NG/UFG) metastable austenitic stainless steels*. Scripta Mater. 63 (11) (2010), pp.1057-1060.

[29] C. Zhu, Z. P. Lu, T. G. Nieh, *Incipient plasticity and dislocation nucleation of FeCoCrNiMn high-entropy alloy*, Acta Mater. 61 (2013) pp. 2993–3001.

[30] E. J. Seo, J.K. Kim, L. Cho, J. Mola, C.Y. Oh, B.C. De Cooman, *Micro-plasticity of medium Mn austenitic steel: Perfect dislocation plasticity and deformation twinning*. Acta Mater. 135 (2017), pp. 112-123.

[31] D. Hua, Q. Xia, W. Wang, Q. Zhou, S. Li, D. Qian, H. Wang, *Atomistic insights into the deformation mechanism of a CoCrNi medium entropy alloy under nanoindentation*, Int. J. Plast. 142 (2021), pp. 102997.

[32] J. R. Morris, H. Bei, G. M. Pharr, E. P. George, *Size effects and stochastic behavior of nanoindentation pop in*, Phys. Rev. Lett. 106 (16) (2011), pp. 1–4.

[33] P. Engels, A. Ma, A. *Hartmaier, Continuum simulation of the evolution of dislocation densities during nanoindentation*, Int. J. Plast. 38 (2012) pp. 159–169.

[34] U. Brückner, A. Epishin, T. Link, Local x-ray diffraction analysis of the structure of dendrites in single-crystal nickel-base superalloys, Acta Mater. 45 (12) (1997), pp. 5223–5231.

[35] A. B. Parsa, P. Wollgramm, H. Buck, C. Somsen, A. Kostka, I. Povstugar, P.P. Choi, D. Raabe, A. Dlouhy, J. Müller, E. Spencer, *Advanced scale bridging microstructure analysis of single crystal Ni-base superalloys*, Adv. Eng. Mater. 17 (2015), pp. 216–230.

[36] G. Laplanche, M. Schneider, F. Scholz, J. Frenzel, G. Eggeler, J. Schreuer, P*rocessing of a single-crystalline CrCoNi medium-entropy alloy and evolution of its thermal expansion and elastic stiffness coefficients with temperature*, Scr. Mater. 177 (2020), pp. 44–48.

[37] H. Mansour, J. Guyon, M. A. Crimp, N. Gey, B. Beausir, N. Maloufi, A*ccurate electron channeling contrast analysis of dislocations in fine-grained bulk materials*, Scr. Mater. 84 – 85 (2014), pp. 11–4.

[38] H. Kriaa, A. Guitton, N. Maloufi, F*undamental and experimental aspects of diffraction for characterising dislocations by electron channeling contrast imaging in scanning electron*, Sci. Rep., 17 (1) (2017), pp. 1-8.

[39] H. Kriaa, A. Guitton, N. Maloufi, *Modeling dislocation contrasts obtained by accurate-Electron Channeling Contrast Imaging for characterising deformation mechanisms in bulk materials*, Materials 12 (10) (2019), pp. 1587.

[40] H. Kriaa, A. Guitton, N. Maloufi, *Modelling electron channeling contrast intensity of stacking fault and twin boundary using crystal thickness effect*, Materials 14 (7) (2021), pp. 1696.

[41] J. Guyon, H. Mansour, N. Gey, M.A. Crimp, S. Chalal, N. Maloufi, *Sub-micron resolution selected area electron channeling patterns*, Ultramicroscopy, 134 (2015), pp. 34-44.

[42] H. Mansour, M.A. Crimp, N. Gey, N. Maloufi, *Accurate electron channeling contrast analysis of a low angle sub-grain boundary*, Scr. Mater. 109 (2015), pp. 76–79.

[43] A. Guitton, H. Kriaa, E. Bouzy, J. Guyon, N. Maloufi, *A dislocation-scale characterisation of the evolution of deformation microstructures around nanoindentation imprints in a TiAl alloy*, Materials 11 (2) (2018) pp. 305.

[44] J. Li, G. Dehm, C. Kirchlechner, *how close can indents be placed without risking an erroneous pop-in statistics? Materialia* 7 (2019), pp. 100378.

[45] F. Habiyaremye, A. Guitton, F. Schäfer, F. Scholz, M. Schneider, J. Frenzel, G. Laplanche, N. Maloufi, *Plasticity induced by nanoindentation in a CrCoNi medium-entropy alloy studied by accurate electron channeling contrast imaging revealing dislocation-low angle grain boundary interactions*, Mater. Sci. Eng. A 817 (2021), pp. 141364.

[46] G. Laplanche, P. Gadaud, C. Bärsch, K. Demtröder, C. Reinhart, J. Schreuer, E.P. George, Elastic moduli and thermal expansion coefficients of medium-entropy subsystems of the CrMnFeCoNi high-entropy alloy, J. Alloys Compd. 746 (2018), pp. 244–255, 2018.

[47] C. A. Schuh, A. C. Lund, Application of nucleation theory to the rate dependence of incipient plasticity during nanoindentation, J. Mater. Res. 19 (7) (2004), pp. 2152–2158.

[48] W. W. Gerberich, J. C. Nelson, E. T. Lilleodden, P. Anderson, J. T. Wyrobek, *Indentation induced dislocation nucleation: The initial yield point*, Acta Mater. 44 (9) (1996), pp. 3585–3598.

[49] J. C. Crone, L. B. Munday, J. J. Ramsey, J. Knap, *Modeling the effect of dislocation density on the strength statistics in nanoindentation*, Model. Simul. Mater. Sci. Eng. 26 (2017), pp. 015009.

[50] P. Hallensleben, F. Scholz, P. Thome, H. Schaar, I. Steinbach, G. Eggeler, J. Frenzel, *On crystal mosaicity in single crystal Ni-based superalloys*, Crystals 9 (3) (2019), pp. 149.

[51] P. Hallensleben, H. Schaar, P. Thome, N. Jöns, A. Jafarisadeh, I. Steinbach, J. Frenzel, *On the evolution of cast microstructures during the processing of single crystal Ni-base superalloys using a Bridgman seed technique*, Mater. Des. 128 (2017), pp. 98–111.

[52] Y. N. Picard, J. D. Caldwell, M. E. Twigg, C. R. Eddy Jr., M. A. Mastro, R. L. Henry, R. T. Holm, *Nondestructive analysis of threading dislocations in GaN by electron channeling contrast imaging*, Appl. Phys. Lett. 91 (2007), pp. 89-92.

[53] M. Ben Saada, N. Gey, B. Beausir, X. Iltis, H. Mansour, N. Maloufi, *Sub-boundaries induced by dislocational creep in uranium dioxide analyzed by advanced diffraction and channeling electron microscopy*, Mater. Charact. 133 (2017), pp. 112–121.

[54] M. Koyama, M. Seo, K. Nakafuji, K. Tsuzaki, *Stacking fault aggregation during cooling composing FCC–HCP martensitic transformation revealed by in-situ electron channeling contrast imaging in an Fe-high Mn alloy*, Sci. Technol. Adv. Mater., 22(1) (2021), pp. 135-40

[55] J. P, Spencer, C.J., Humphreys, P.B. Hirsch, *A dynamical theory for the contrast of perfect and imperfect crystals in the scanning electron microscope using backscattered electrons*,

Philos. Mag. 26 (1) (1972), pp. 193-213

[56] D. Hull, D.J. Bacon, *Introduction to dislocation*s, Fourth ed., Butterworth-Heinemann, Oxford, 2001.

[57] B. Pang, I. P. Jones, Y. L. Chiu, J. C. F. Millett, G. Whiteman, *Electron channelling contrast imaging of dislocations in a conventional SEM*, Philos. Mag. 97 (5) (2017), pp. 346–359.

[58] K. L. Johnson, *Contact Mechanics*. Cambridge University Press, 1985.

[59] J.P. Hirth; J. Lothe, Theory of dislocations, Second edi. John Wiley & Sons, Inc, Hoboken, USA, 1982.

[60] T. A. Michalske, J. E. Houston, *Dislocation nucleation at nano-scale mechanical contacts*, Acta Mater. 46 (1998), pp. 391–396.

[61] Y. L. Chiu, A. H. W. Ngan, *Time-dependent characteristics of incipient plasticity in nanoindentation of a Ni3Al single crystal*, Acta Mater. 50 (6) (2002), pp. 1599–1611.

[62] H. S. Leipner, D. Lorenz, A. Zeckzer, H. Lei, P. Grau, *Nanoindentation pop-in effect in semiconductors*, Phys. B: Condens. Matter 308–310 (2001), pp. 446–449.

[63] J. K. Mason, A.C. Lund, C. A. Schuh, *Determining the activation energy and volume for the onset of plasticity during nanoindentation*, Phys. Rev. B. 73 (2006), pp. 1–14.

[64] R. J. Wagner, L. Ma, F. Tavazza, L. E. Levine, *Dislocation nucleation during nanoindentation of aluminum*, J. Appl. Phys. 104 (2008), pp. 114311.

[65] C. Caër, E. Patoor, S. Berbenni, J.S. Lecomte, *Stress-induced pop-in and pop-out nanoindentation events in CuAlBe shape memory alloys*, Mater. Sci. Eng. A 587 (2013), pp. 304–312.

[66] L. Zhang, T. Ohmura, *Plasticity initiation and evolution during nanoindentation of an iron-3% silicon crystal*, Phys. Rev. Lett. 112, (14), (2014), pp. 1–5.

[67] A. M. Minor, E. T. Lilleodden, E. A. Stach, J. W. Morris, *Direct observations of incipient plasticity during nanoindentation of Al*, J. Mater. Res., 19 (2004), pp. 176–182, 2004.

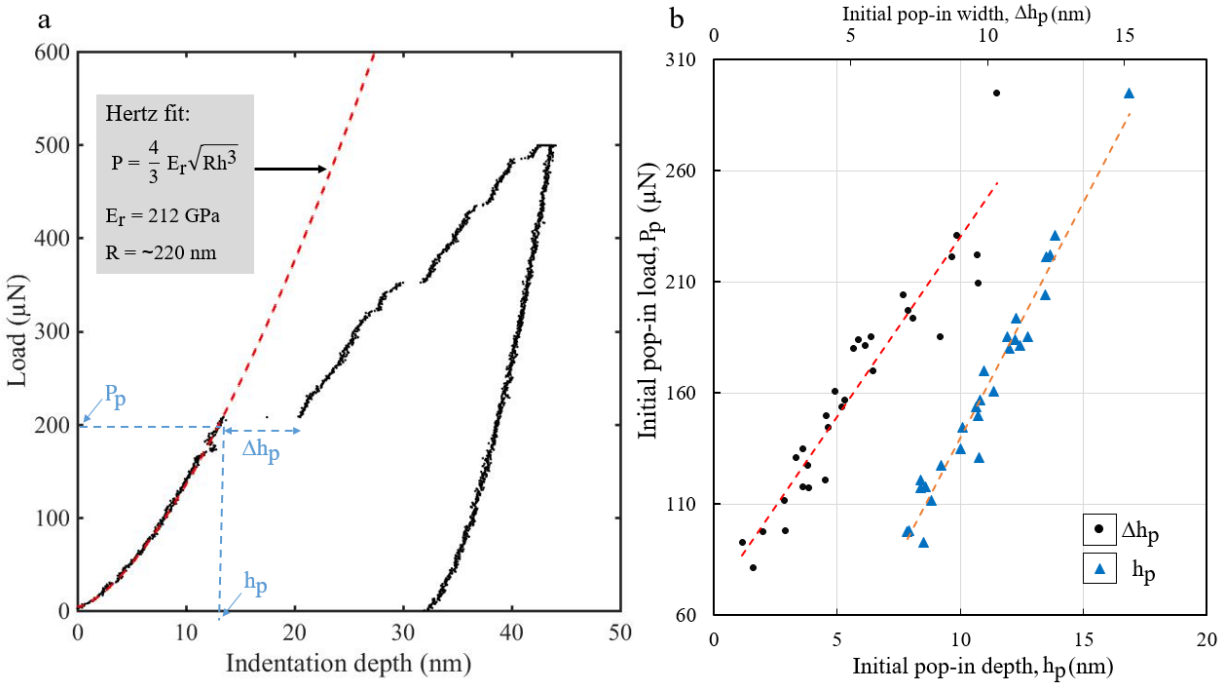

Figure 1. (a) A typical load-displacement curve on a single crystal for a maximum load of 500 μN. The red dashed line represents the fit to the theoretical Hertz elastic contact solution. (b) A plot of the initial pop-in load (P_p) against the pop-in depth (h_p) and pop-in width (Δh_p) for several indentations in the single crystal.

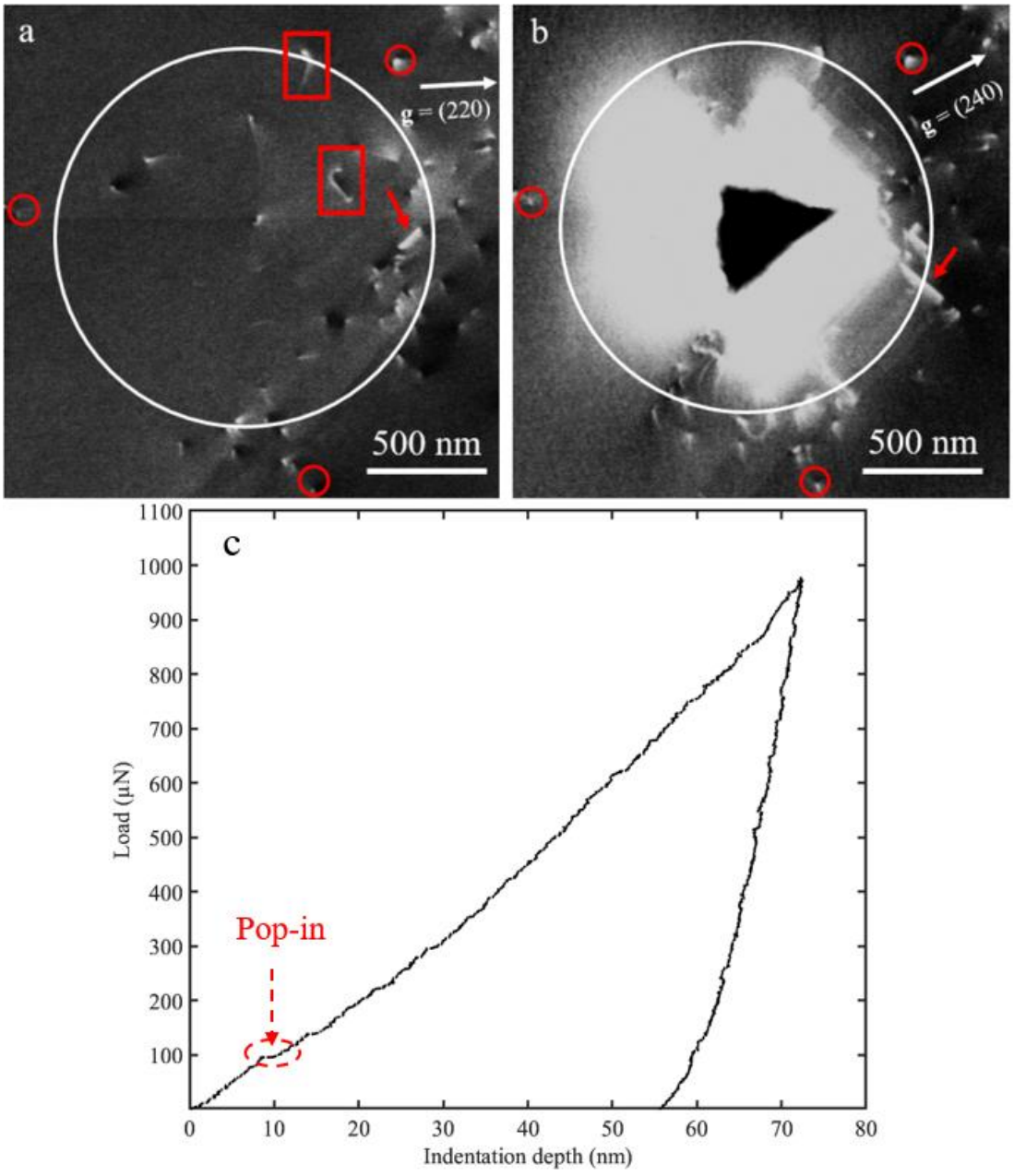

Figure 2. ECC micrographs of localized microstructure (a) before and (b) after nanoindentation. Red circles in Figs. 1a-b enclose reference dislocations that are used to show that the two images are taken in the same region. Red arrows show stacking faults. White circles show the regions from which ρ_{loc} is determined. Red rectangles show non-threading dislocations. (c) Plot of load-indentation depth for nanoindentation in Fig. 2b.

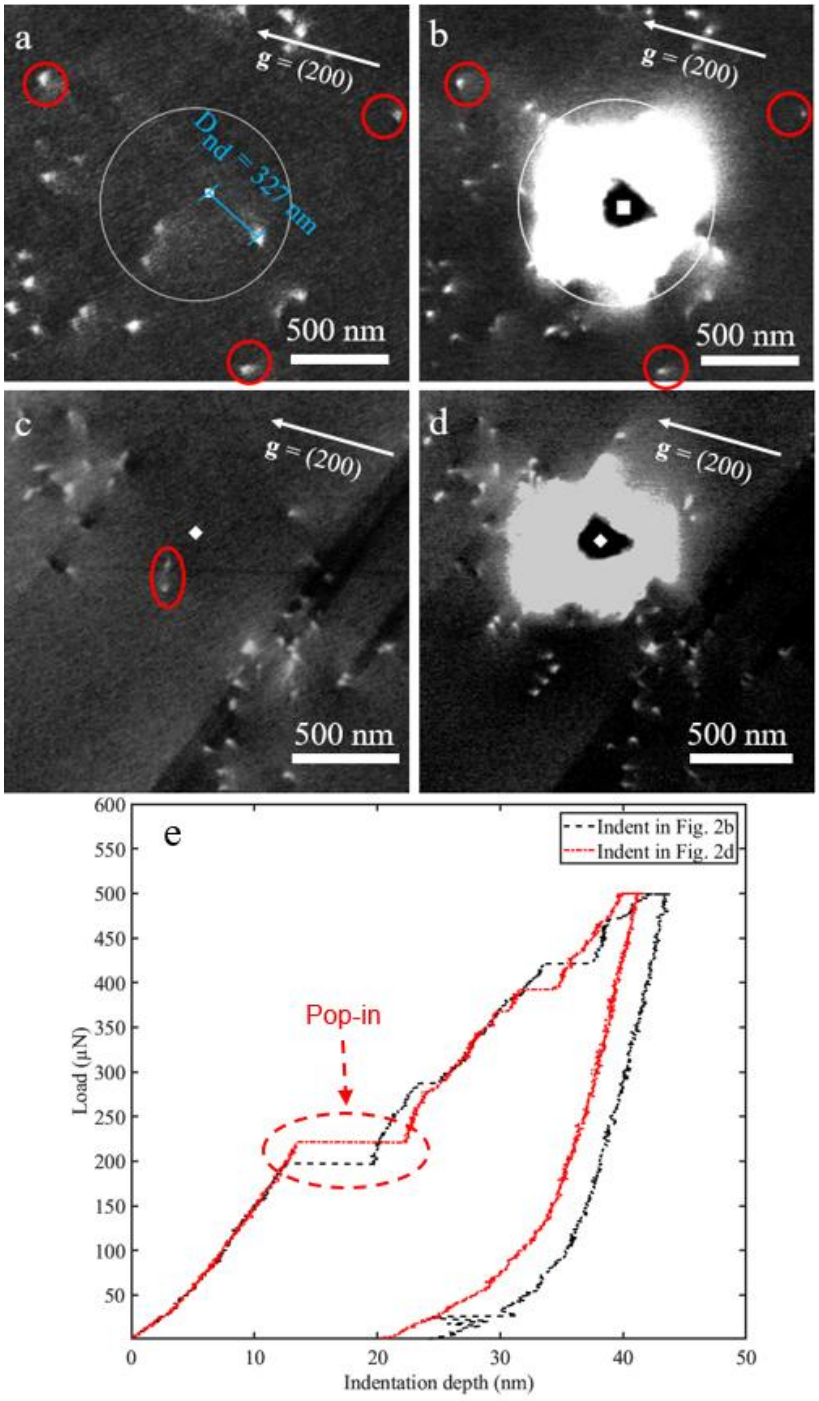

Figure 3. ECC micrographs (a) before and (b) after nanoindentation up to a maximum load of 500 μN for diffraction vector, g = (200). The blue segment represents the distance between the nanoindentation axis and the nearest dislocation (D_{nd}). Red circles are reference dislocations that show that the micrographs were taken in the same region. ECC micrographs (c) before and (d) after nanoindentation for interacting dislocations. Red ellipses enclosed the interacting dislocations that can be either a pair of dislocations or a dislocation dipole. (e) Plots of load-indentation depth for nanoindentation in Figs. 3b and 3d, respectively.

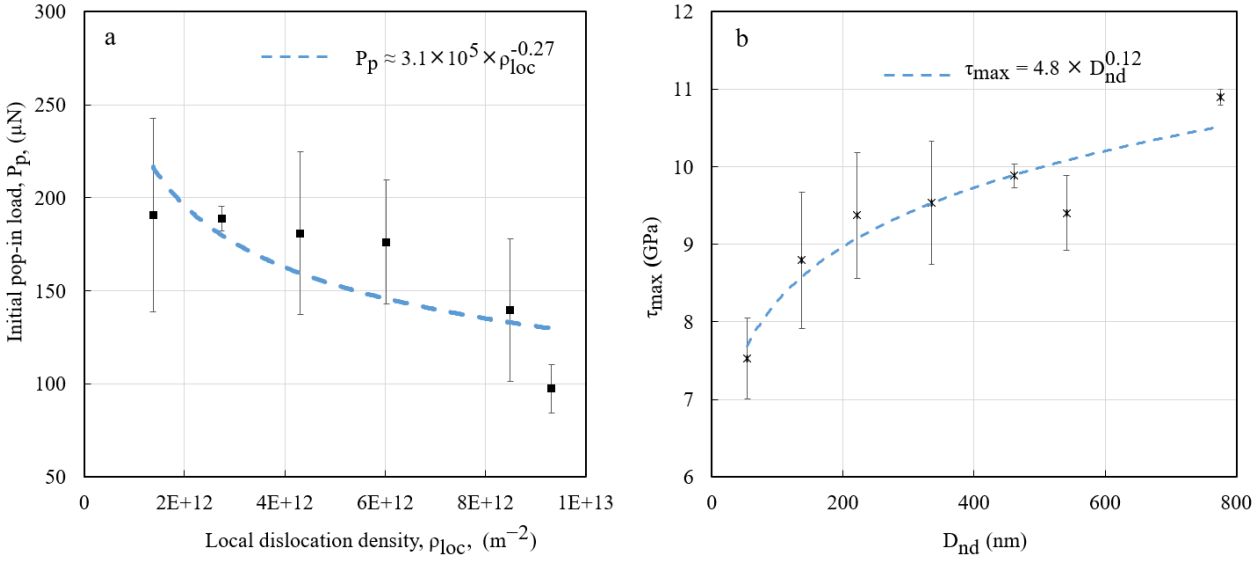

Figure 4. (a) A plot of the initial pop-in load (P_p) against the pre-existing local density of dislocations (ρ_{loc}). (b) A plot of the maximum shear stress at the pop-in (τ_{max}) estimated by equation 4 against the distance from the indentation axis to the nearest dislocation (D_{nd}). Bars in (a) are built based on the mean ± standard deviation of P_p for each ρ_{loc} value. Bars in (b) are built based on the mean ± standard deviation of τ_{max} for each D_{nd} value. The detailed Figs. 4a-b are depicted in Fig. S1 (supplementary data) and Fig. 5a, respectively.

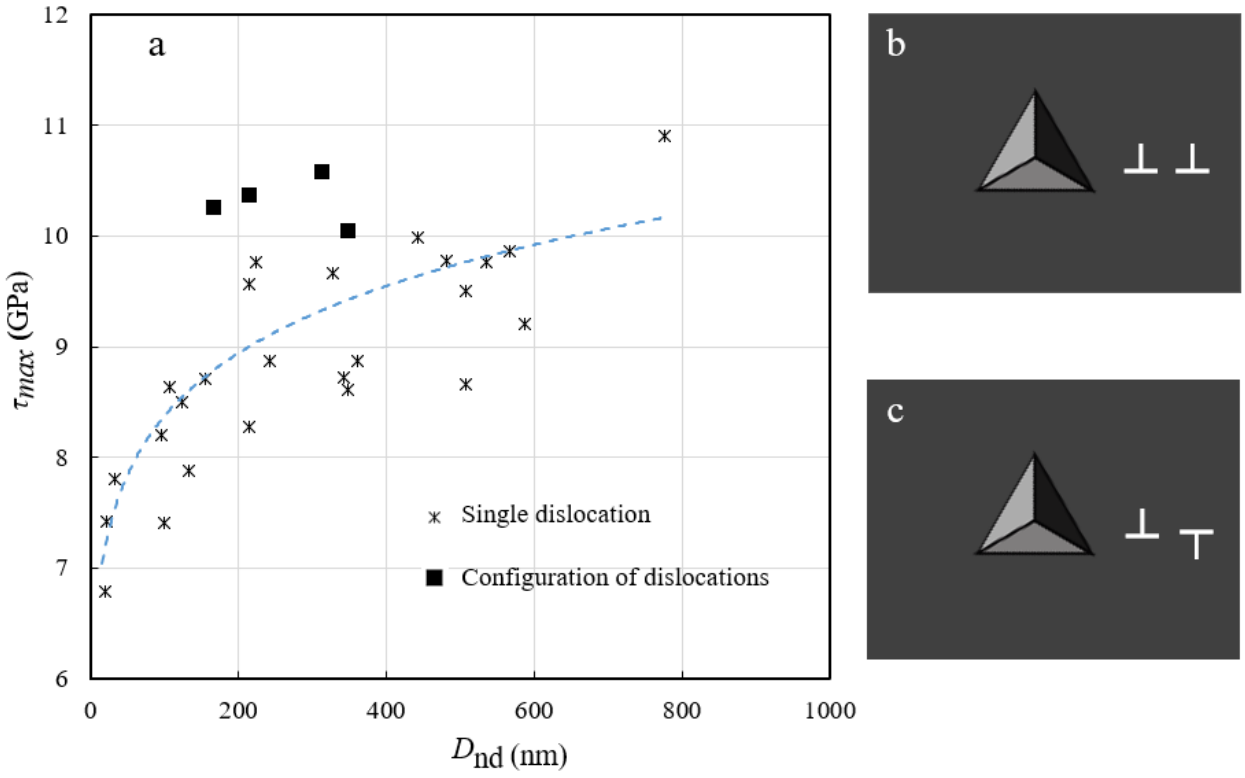

Figure 5. (a) A plot of maximum shear stress at the pop-in (τ_{max}) against distance from the nanoindentation axis to the nearest dislocation (D_{nd}). It shows the difference between single dislocations and the configuration of dislocations represented in (b) a pair of dislocations and (c) for a dislocation dipole. The symbols ⊥ are used to mark the positions of dislocations and do not refer to their type.

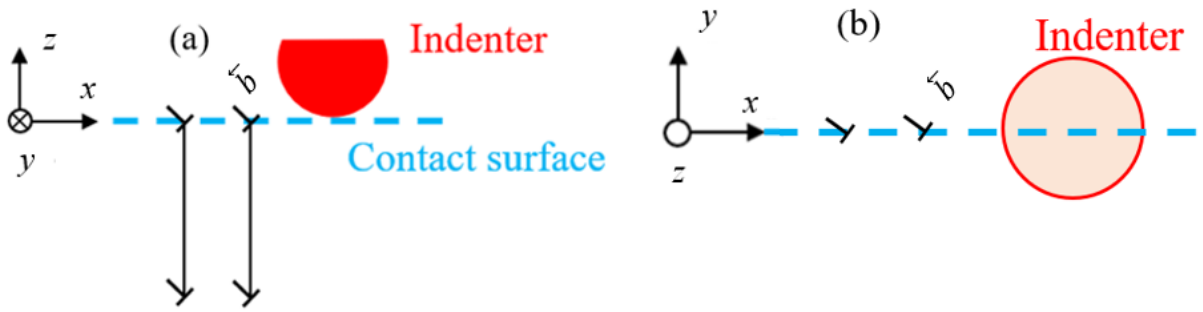

Figure 6. A Schematic representation of dislocation configurations used for the stress field calculations: (a) plane *x*-*z* showing a pair of dislocations with a line direction parallel to *z*, (b) plane *x*-*y* showing Burgers vector (b) of a pair of dislocations at a 54° to *x*. Dislocations are marked by the edge dislocation symbol and the arrow shows the direction of the Burgers vector. The right-hand/finish-start convention was used to represent dislocations.

Table 1. Materials parameters used for elastic calculations

Parameters	Values
Materials	CrCoNi single crystal
Orientation	[001] // *z*
Crystal structure	Face Centered Cubic (FCC)
Lattice parameter (nm)	0.357
Burgers vector magnitude (**|b|, *nm***)	0.2524

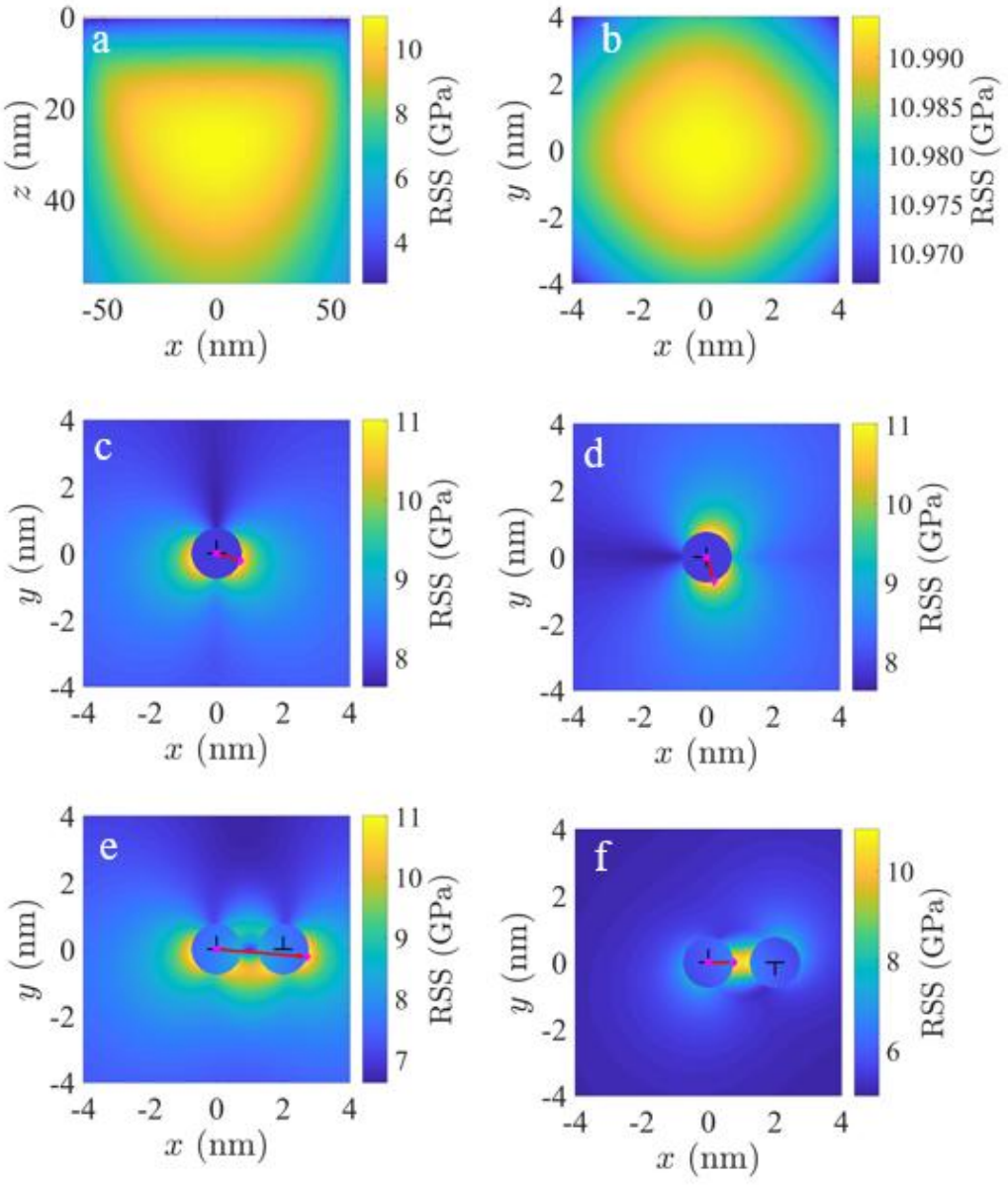

Figure 7. Contour plots showing the distribution of RSS due to (a-b) indentation alone, (c-d) indentation and a single dislocation with **b** = ½ [10-1] and **b** = ½ [011] (e) indentation and a pair of dislocation with **b** = ½ [10-1], (f) indentation stress and a dipole with (***b*** = ½ [10-1] and **b** = ½ [-101]). The purple-red circle and diamonds linked by a line show the positions of the center and the MRSS value. The dislocation core region is defined as the cut-off radius, $r_0 = 3|\boldsymbol{b}|$. The r_0 is estimated as a value that gives reasonable values of τ_{max} comparable to experiments.

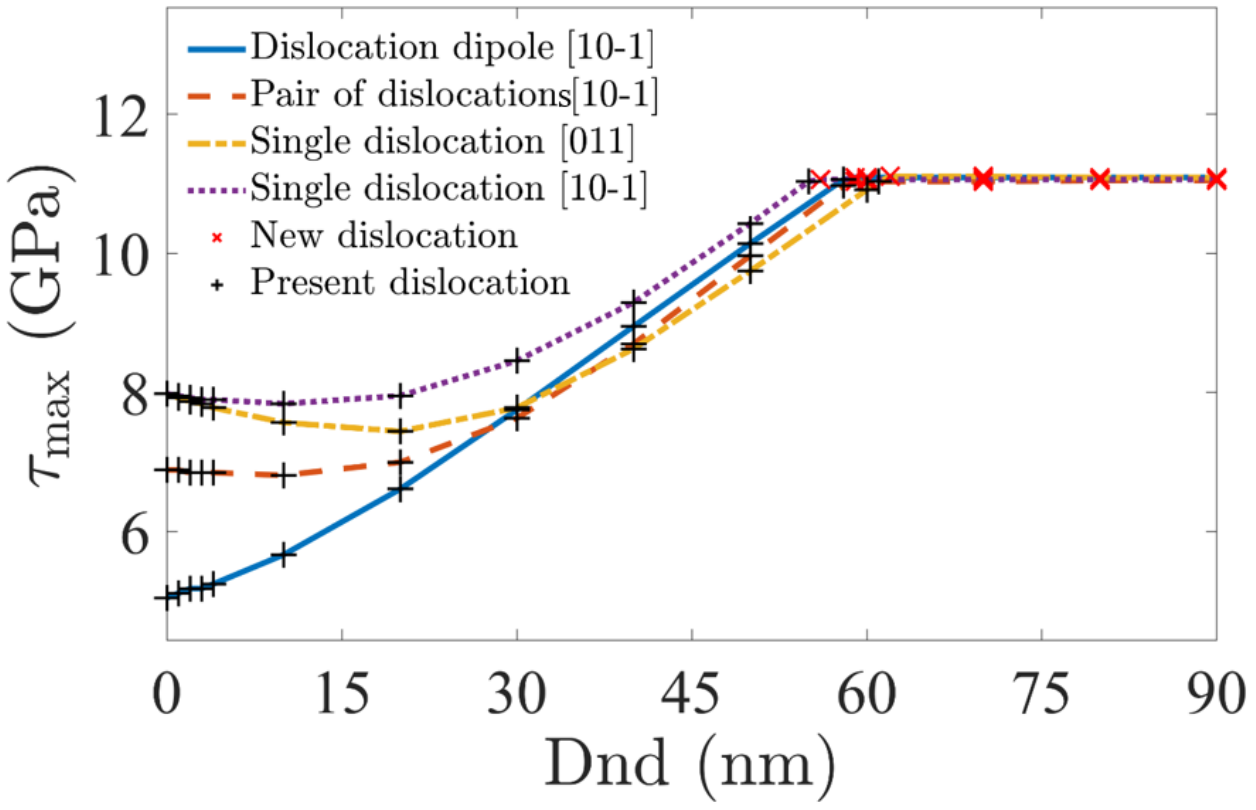

Figure 8. A plot of maximum shear stress (τ_{max}) against distance from the nanoindentation axis to the nearest dislocation (D_{nd}) for different configurations of dislocations obtained from stress field calculations.